Amino-grafting pre-functionalization of terephthalic acid by impulse dielectric-barrier discharge (DBD) plasma for amino-based Metal-Organic Frameworks (MOFs)

Aymane Najah, Dimitri Boivin, Cédric Noël, Ludovic de Poucques, Gérard Henrion, Stéphane Cuynet

Amino-grafting pre-functionalization of terephthalic acid by impulse dielectric-barrier discharge (DBD) plasma for amino-based Metal-Organic Frameworks (MOFs)

Aymane Najah*, Dimitri Boivin, Cédric Noël, Ludovic De Poucques, Gérard Henrion, Stéphane Cuynet

[1] Université de Lorraine, CNRS, IJL, F-54000 Nancy, France

e-mail : aymane.najah@univ-lorraine.fr

Abstract

The pre-functionalization of organic ligands before MOFs synthesis has been widely carried out via wet-chemical methods. A possible novel route to perform the pre-functionalization of MOFs' organic ligands is to graft amino groups on the ligand by means of plasma treatments. In this study, a NH_3 impulse dielectric-barrier discharge plasma treatment is used to investigate the efficiency of the pre-functionalization of terephthalic acid. For this purpose, plasma diagnostics is coupled with material characterizations to identify the main reactive plasma species involved in the ligand functionalization. The presence of NH radicals in the plasma phase together with structural modification evidence the effect of the plasma treatment. Chemical analyses of the treated material confirm the presence of nitrogen in the treated sample and prove that the grafting of the amino group occurs at the functional carboxyl group (-COOH) of terephthalic acid, by substituting the C–OH bond by C-NH_2 bond. All these results indicate

successful modification of terephthalic acid by grafting amino groups thanks to the plasma treatment.

Keywords: Terephthalic acid, MOFs, pre-functionalization, plasma, DBD, NH_3, grafting, amino groups.

1. Introduction

Considered as among the most promising novel materials because of their wide versatility, Metal-Organic Frameworks (MOFs), also known as porous coordination polymers are porous hybrid compounds formed by self-assembly of metal clusters (secondary building units (SBU)) with polytopic organic ligands to form crystalline networks [1-3]. MOFs exhibit great diversity in terms of structure and composition. Therefore, their intrinsic nature gives them impressive features, in particular high porosity with a wide range of pore size and high internal surface area [4]. These traits make them attractive across a wide range of applications, such as gas storage and separation [5-7], catalysis [8-10], sensing [11-13], optics [14-16], batteries [17-19], among many other fields.

In addition to the wide variety of combinations of organic and inorganic entities used to design MOFs with desired topologies and characteristics, their properties can also be modulated or even enhanced by tuning the surface chemistry via functionalization process. Usually, the functionalization process of MOFs is carried out via wet-chemical methods [20-22]. There are two main routes to prepare functionalized MOFs:

(i) pre-functionalization that involves the addition of functional groups into the phenyl ring of the organic ligand. This effective tool was initially developed by the group of O. Yaghi [23] who synthesized a series of isoreticular MOFs (IRMOFs) by grafting some functional groups, such as -Br, -NH_2, -OC_3H_7, OC_5H_{11} in the organic ligand (terephthalic acid) of MOF-5. In this way, other series of MOFs with different organic functionalities and isostructural topologies were synthesized, like the series of MIL-53-X_n (X_n = Cl, Br, NH_2) of Férey *et al.* [24].

(ii) Post-synthetic modification of MOFs, initially suggested by Hoskins and Robson [25], which occurs by chemical modification of the network after the synthesis [26-28]. The main strategies for functionalization of MOFs by post-synthetic modification include

covalent, dative modifications and those by encapsulation [29-31]. The scope of this paper relates to the pre-functionalization of the organic ligand.

In the literature, several computational and experimental studies of MOFs' functionalization report on the effectiveness of introducing specific substituent groups on the ligand structure. It was shown that grafting functional groups, such as amino groups on the aromatic ligand, enhances the selectivity of MOFs toward certain gases, and improves the interaction between the adsorbent and adsorbate, particularly for CO_2 and H_2 [32-34]. Therefore, many works have been carried out to improve the CO_2 uptake on MOFs. Rada *et al.* [35] studied the CO_2 adsorption on amino functionalized titanium-based MOFs, NH_2-MIL-125 (Ti), and compared it with the pristine material MIL-125 (Ti). These authors pointed out that the addition of amino functional group increases remarkably the CO_2 uptake and affinity, with an adsorption capacity of 10.76 mmol/g and 8.9 mmol/g at 273 K and 298 K, respectively, much higher than those of untreated MIL-125 (Ti) (4 mmol/g and 2,8 mmol/g at 273 K and 298 K, respectively). As for H_2 uptake, Klopper *et al.* [36] showed that grafting an electron-donating radical such as amino into the phenyl ring of the organic ligand improves the energy of interaction of H_2 with the phenyl ring. Wu *et al.* [34] studied sorption enthalpy of MIL-68 (In) and an amino functionalized MIL-68 (In). They showed that the amino group in NH_2-MIL-68 (In) could indeed improve the adsorption kinetics of H_2 on the material. Besides gas storage/selectivity improvements of some MOFs by amino functionalization, this latter can also enhance their tailorability toward drug/gene delivery [37-40], asymmetric catalysis [41-43], tissue engineering [44-46], etc.

Besides the wet chemical methods, a third possible route to functionalize MOFs consists in using low temperature plasma treatments. Plasma treatments are widely used to functionalize different materials like polymers [47-49], cotton [50-52], wood [53-55], glass [56-58], metals [59-61]. The dry plasma processes used for the elaboration and functionalization of materials are varied. In fact, they differ according to the gas pressure, ranging from low pressure

processes (a few Pa to 100 Pa) [48, 54, 62-64] to atmospheric pressure processes [49, 51, 55-57, 65]. Low-pressure plasma processes are highly non-equilibrium thermodynamics means with high electron temperatures that can reach a few tens of electron-volts and a low degree of ionization [66]. On the other hand, plasmas at atmospheric pressure can have a high degree of ionization but low electron temperatures [67]. Therefore, the pressure difference from one process to another plays a major role in the physical and chemical actions the plasma will have on the targeted material. Indeed, plasma processes provide treatments at non-equilibrium thermodynamic state, thus allowing novel reaction possibilities. The assets of these cold plasma treatments are based on factors such as:

(i) The bombardment of the surface of a material by energetic species of the plasma, which generates a breaking of some covalent bonds and the formation of free radicals. These radicals react with the active species of the plasma, which results in the formation of functional chemical groups on the surface of the materials depending on the nature of the gas phase.

(ii) Plasma treatments can be carried out in dry conditions, thus reducing the use of chemicals and solvents, and therefore the energy to recycle or eliminate the residues.

(iii) Consequently, from a security point of view, there is less vulnerability to chemical risks with plasma treatments, compared to the wet chemical methods.

In this paper we report on a novel pre-functionalization process by a dry chemical method using a dielectric barrier discharge (DBD) plasma treatment of terephthalic acid ($C_6H_8O_4$). This acid is known as the major organic ligand used for MOFs' synthesis due to its rigidity, its variety of architectures, and its versatile coordination modes. Although there are many studies focusing on the MOFs' functionalization, none of these studies concerns the plasma functionalization. Therefore, the scope of this study is to examine and evaluate the efficiency of the DBD plasma treatment to realize a pre-functionalization by grafting amino groups on the organic ligand. The idea is first to have a proof of concept of the feasibility of the dry chemical pre-functionalization

via DBD treatment on the organic ligand, and second to evaluate the efficiency of the DBD plasma treatment for MOFs functionalization. Therefore, plasma diagnostics and material characterization are carried out to examine the evolution of the plasma discharge during the treatment, to determine the chemical species present in the plasma, and to check the efficiency of the grafting process.

2. Experimental section

2.1. DBD setup and material

A schematic diagram of the experimental setup is illustrated in figure 1. The DBD system is set up in a typical planar symmetric configuration of two dielectric plates of square shape placed opposite to each other. A copper electrode is placed on the backside of each dielectric plate. The upper square electrode of 10 cm^2 is connected to the high voltage while the lower electrode with same external dimension is grounded (electric reference potential of the system). The lower electrode has a specific geometry with a specific surface area of about 8 cm^2, allowing to confine the powder regardless the effect of the electric field on the powders during the plasma discharge. For the plasma treatment, the sample is spread on the bottom dielectric. The dielectrics plates are made of aluminium nitride for its high electrical resistivity (> 10^{13} Ω.m); it is also primarily used to prevent any oxygen poisoning of MOFs that could happen during plasma treatments by using alumina or silica as dielectrics. The dimensions of the square shape dielectrics are 5 x 5 cm^2 and 1 mm in thickness. The DBD cell is fixed on PTFE supports to make it electrically insulated from the surrounding parts of the whole system.

The electrical system consists of two high voltage generators (Technix SR15-R-1200) connected to a switcher (BEHLKE HTS 301-03-GSM) that allows applying the voltage alternatively to each of the electrodes at a maximum frequency of 4 kHz. The switcher is connected to two 33 Ω current limiting resistors. A low frequency function generator (Yokogawa FG120) triggers the switcher to deliver the suitable waveform with the desired

frequency. The plasma discharge is generated with a symmetric square pulse voltage of 6 kV_{p-p} (+3 kV, -3 kV), at a frequency of 4 kHz, for one hour of treatment. The square waveform, as a matter of a fact, is used to reduce the discharge duration, and thus allows preventing eventual arc discharges that could deteriorate the sample. A linear motion device allows adjusting the gap width between the two dielectric plates. All experiments are carried out with a gap of 3 mm between the dielectrics.

The whole DBD system is placed inside a spherical stainless-steel chamber of 60 L in volume. It allows working under controlled atmosphere and pressure. The chamber is connected to a pumping system that consists of a primary vacuum pump to reach a pressure down to 10^{-1} Pa, and a turbomolecular pump to reach 10^{-4} Pa residual pressure. All experiments reported here were carried out within a static gas inlet regime at a constant pressure of 10^{4} Pa. This means that prior to the DBD plasma ignition, the chamber was evacuated down to 10^{-4} Pa and then filled with ammonia gas (Air Liquide, 99.9% purity). As soon as the pressure reached 10^{4} Pa, the gas-in and gas-out valves were closed, thus maintaining a static atmosphere in the chamber. Working in a static atmosphere in the chamber allows preventing scattering occurrence on the powder to be treated.

The commercial terephthalic acid used for this study is a white organic crystalline powder with formula $C_6H_4(COOH)_2$. According to the supplier (Sigma Aldrich), this material has over 98% purity, a density of 1.58 g/cm^3 at ambient temperature, a molecular weight of 166.13 g/mol and a melting point at 300 °C.

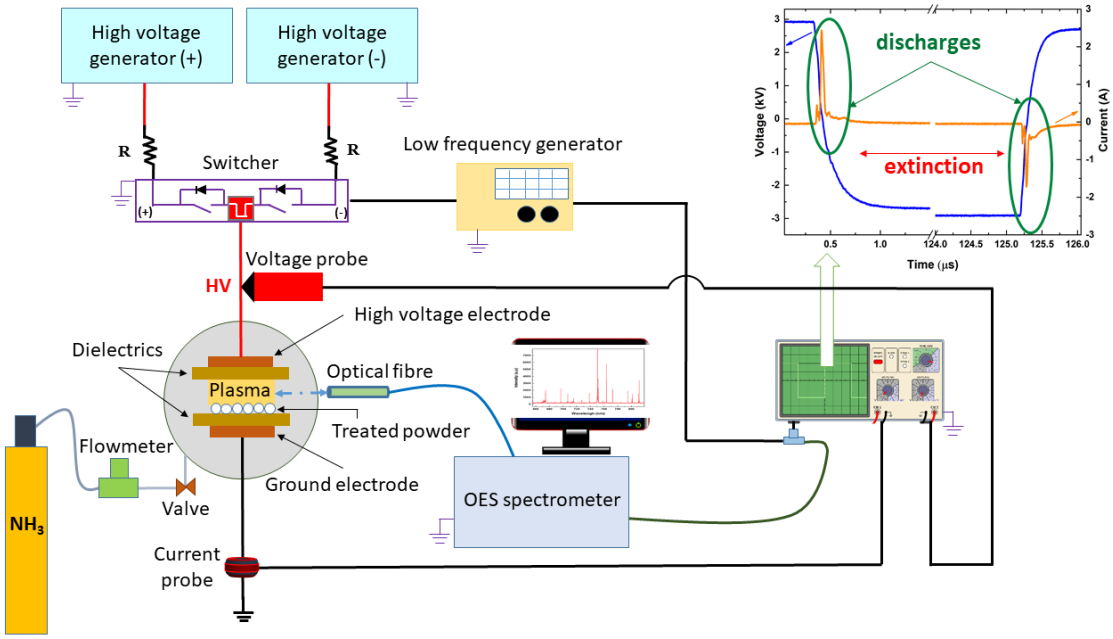

Figure 1. *Schematic diagram of the experimental setup of the DBD plasma treatment with electrical and optical diagnostics.*

2.2. Characterization

2.2.1. Plasma diagnostics

- **Electrical measurements**

During the plasma treatment of terephthalic acid, the discharge voltage and current were measured by a voltage probe (Cal Test CT4028, with a bandwidth from DC to 220 MHz) and a current probe (Magnelab CT-D1.0-B, with a bandwidth between 200 Hz and 500 MHz), respectively. An oscilloscope (LeCroy 104Xi) monitored the electrical characteristics.

- **Optical emission spectroscopy**

Optical emission spectroscopy (OES) measurements during the DBD treatment were performed with a Jobin-Yvon Triax 550 spectrometer equipped with a 1200 grooves mm^{-1} grating and an intensified charged couple device camera (ICCD). The light emitted by the plasma was collected through a quartz window via an optical fibre facing the discharge. The distance

between the centre of the plasma and the optical fibre is 27 cm. The emission spectra were recorded between 250 nm and 700 nm, with a spectral resolution of 0.07 nm. In order to synchronize the OES measurements with the discharge pulses, the TTL signal that triggers the DBD high voltage also served to externally trigger the ICCD detector. The latter was operated in gated mode with a gate pulse width set at 5 µs. This allows collecting light signal during the current pulse and also during the temporal post-discharge whose duration, in our case, is estimated at 5 µs. Beyond 5 µs after each DBD impulses, the light emission coming from the plasma source becomes negligible. Therefore, the OES measurement is set up to obtain the best signal-to-noise ratio. The measurements were averaged over 200 000 discharge pulses to further improve this signal-to-noise ratio.

2.2.2. Material characterization

- **X-Ray diffraction (XRD)**

The structural characterization was carried out at room temperature by a Panalytical X'Pert Pro MPD diffractometer, using Cu $K_{\alpha 1}$ (λ= 1.5406 Å) radiation, operated at a voltage of 40 kV and a current of 40 mA, in a Bragg-Brentano geometry. The diffractometer is equipped with a goniometer theta/theta, a hybrid monochromator, an X'celerator linear detector type and a sample spinning. The diffraction patterns were recorded over a 2θ range between 10 and 40°, with a scan rate of 4 °/min and a step size of 0.02°. The powder samples were prepared on a silicon zero-background sample holder.

- **Thermogravimetric analysis-mass spectrometry (TGA-MS).**

The thermogravimetric measurements, coupled with a mass spectrometer, were performed using a thermogravimetric analyser (SETARAM Setsys Evolution) and a mass spectrometer (OmniStarGSD301C-Pfeiffer Vacuum). An amount of 19 mg for each sample was prepared in a platinum crucible. The TGA-MS analysis were carried out in the temperature range of 20-400 °C under a constant helium gas flow (20 mL.min^{-1}), at a heating rate of 5 °C min^{-1}.

- **X-Ray photoelectron spectroscopy (XPS)**

The chemical analysis of the samples was analyzed by using a Thermo Fischer scientific ESCALAB Xi^+ X-ray photoelectron spectrometer (XPS) equipped with an Al Kα monochromator. The area of the analysis is 900 x 900 μm^2 survey scans (0 - 1350 eV) were carried out for each sample, in CAE (constant analyzer energy) mode, with a pass energy of 200 eV and a step size of 1 eV. Narrow scans (C_{1S}: 280-298 eV, O_{1S}: 525-545 eV, N_{1S}: 392-410 eV) were done at pass energy (CAE) of 20 eV, and step size of 0.1 eV.

3. Results and discussions

3.1. Voltage-current characteristics

Figure 2 shows the time evolution of the applied voltage and the discharge current during the DBD treatment. A current measurement without the powder (equivalent to t = 0 min) is also presented in the figure to compare the powder effect on the discharge current. Based on the voltage curve, a value of 2 kV of voltage is sufficient to ignite the plasma. As for the discharge current, its maximum peak current has a duration Δt_1 = 75 ns. Moreover, the maximum of the current intensity increases throughout the treatment. Between the beginning (t = 0 min) and the end of the treatment (t = 60 min), the current passes in positive and negative polarities from 2.46 A to 2.80 A, and from -1.75 A to -2.13 A, respectively. The rise in the current absolute values could be attributed to the change of the secondary electron emission yield, induced by the bombardment of the organic ligand by the free electrons and ions, which develops throughout the discharge. A study reported by N. Bundaleska et al. [68] has shown that graphene's secondary emission yield has changed while doping the material with nitrogen by a plasma treatment; however no current-voltage characteristics were made in this study. The asymmetric nature of the two electrodes could justify the difference in the absolute current values between the positive and the negative polarities. Moreover, it is clear that the current values of the DBD treatment without powder and with the presence of powder are not the same.

In fact, the current value decreases when adding the powder by a factor of 0.28 and 0.32 in positive and negative polarities, respectively. Indeed, the addition of an insulating powder in the system induces a change in the dielectric constant of the system, and hence could influence the current characteristics of the DBD discharge. Nevertheless, the addition of the powder between the dielectrics does not change the breakdown conditions of the discharge. Consequently, the breakdown mechanism with positive and negative pulses can be slightly different. Compared to conventional sinusoidal voltage DBD sources for which the measured current is relatively low (in the range of mA), the unusual high values of the measured current in our case of impulse DBD can be obtained since the current is proportional to the very fast time variation of the voltage V with time (dV/dt). Therefore, the rapid fall and rise of the voltage to a maximum value within the square waveform induces higher current values (in the range of A). In addition, the calculation of the integral of the current pulse over the main plasma discharge time (Δt_2 ~350 ns) show that the cumulative amount of electrical charges in positive and negative polarities is quite the same with a value of about 1.3 10^{-7} C during plasma treatment of powder, irrespective of the polarity of the voltage pulse. In addition, the shape of the current curves is mostly dependant on the electrode shape and on the presence or not of terephthalic acid powder. Furthermore, the shape of the discharge current remains globally the same all over the 60 minutes of the powder plasma treatment, showing that the consumption of the NH_3 in the discharge is insignificant compared with the global gas volume of ammonia present in the reactor. Hence, it does not affect the plasma conditions of the discharge and the material is treated in the same conditions throughout the plasma treatment.

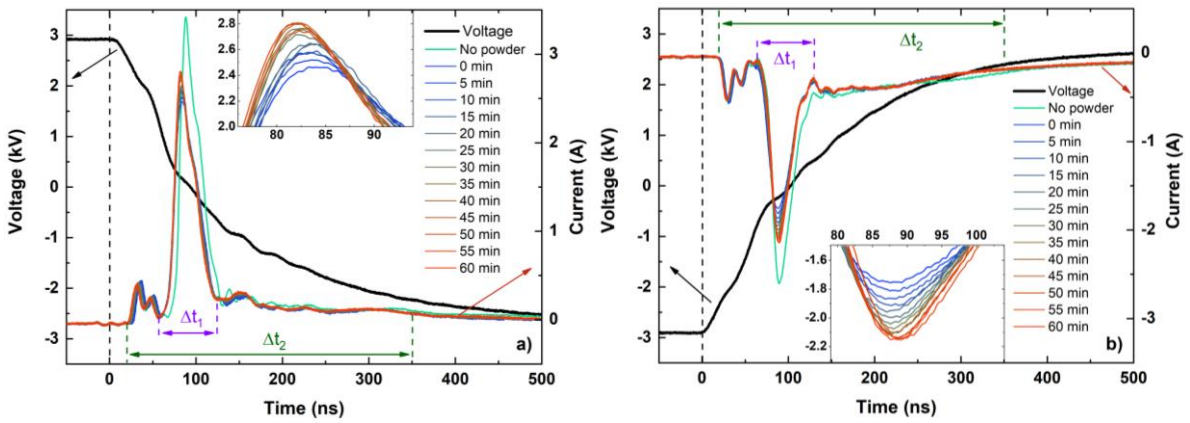

Figure 2. *Current-Voltage measurements of the DBD plasma treatment of terephthalic acid at 6 kV_{pp} voltage, pressure of 10^4 Pa, frequency of 4 kHz, and 3 mm of inter-electrode distance. a) falling edge of the voltage, b) rising edge of the voltage. Current measurement without terephthalic acid (green curve) is also shown.*

3.2. Optical emission spectroscopy

The optical emission spectrum obtained during the DBD treatment of terephthalic acid is shown in figure 3. The spectrum exhibits several atomic and molecular emission lines resulting from the dissociation of ammonia molecules. The main features of the spectrum are the presence of molecular nitrogen illustrated by the emission of the second positive system of N_2 ($C\ ^3\Pi_u \rightarrow B^3\Pi_g$) with a dominant emission band head at 337 nm, and a peak at 336 nm attributed to the NH ($A^3\Pi \rightarrow X^3\Sigma^-$) band transition [69]. Atomic hydrogen transition belonging to the Balmer series (H_α, 656 nm) is observed as well. This implies that the free NH radicals present in the plasma can possibly interact with the materials and could be grafted onto it. Furthermore, an intense emission band is observed around 563-567 nm that likely belongs to the Schuster's system of the NH_3 molecule [70, 71].

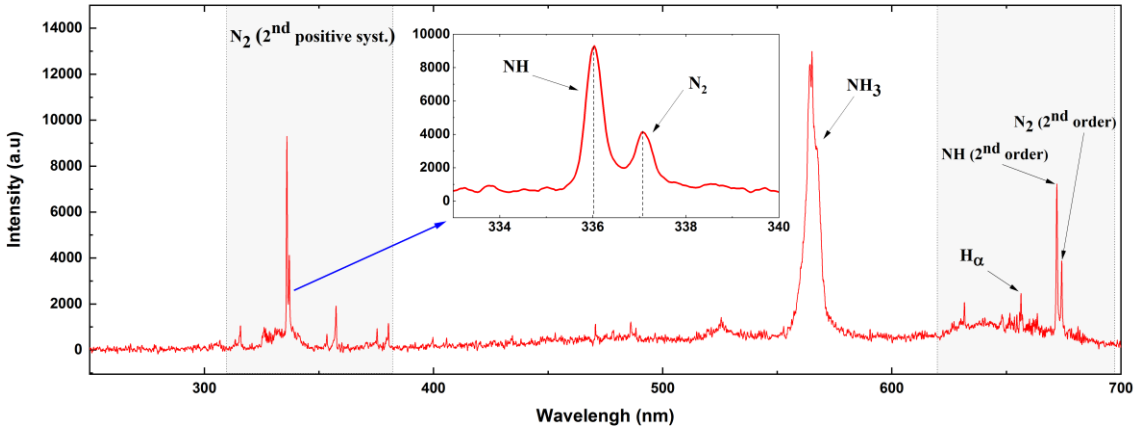

Figure3. *OES spectrum of terephthalic acid treated by DBD in NH_3, at 6 kV_{pp} voltage, pressure of 10^4 Pa, frequency of 4 kHz, and 3 mm of inter-electrode distance.*

3.3. X-Ray diffraction

Figure 4 shows the XRD patterns of terephthalic acid and terephthalic acid treated by DBD. The powder diffraction database (PDF-4) was used for the phase identification. The XRD pattern of terephthalic acid sample matches well with the reference pattern of terephthalic acid phase (PDF 00-031-1916), thus confirming the purity of the material. New peaks corresponding to a second phase are revealed in the sample treated by DBD. Indexation of these diffraction peaks (see table 1 and fig. 4) shows that this new phase corresponds to ammonium hydrogen terephthalate (PDF 00-052-2145). More data about the crystal structure of ammonium hydrogen terephthalate can be found in the paper of R.E. Cobbledick and R.W. Small [72]. The lattice parameters of terephthalic acid and ammonium hydrogen terephthalate are given in table 2. This clearly indicates that the plasma treatment as reported here implies structural modifications of the organic ligand.

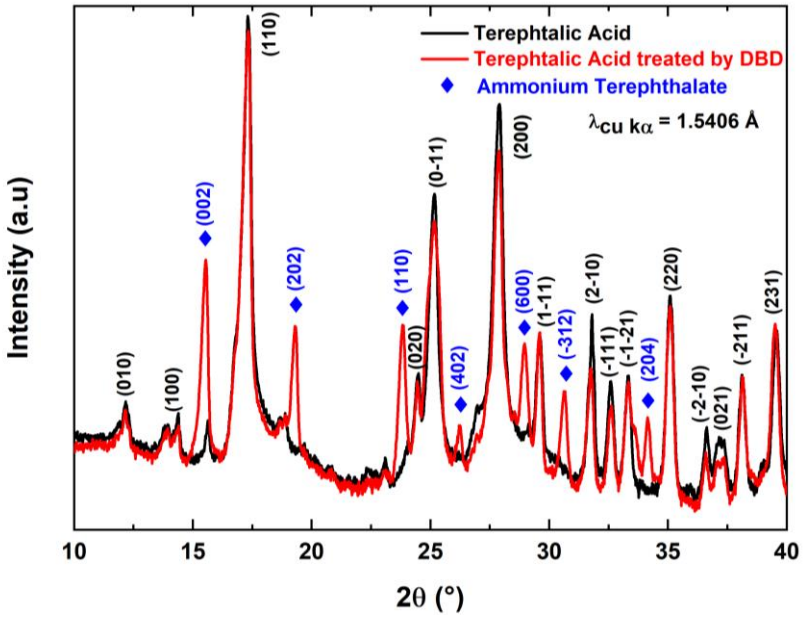

Figure 4*. XRD patterns of terephthalic acid and terephthalic acid treated by DBD.*

Table 1. *Indexation of diffraction peaks of terephthalic acid treated by DBD shown in figure 4.*

2θ (°)	15.54	19.31	23.83	26.23	28.96	30.66	34.15
d (Å)	5.68	4.58	3.72	3.38	3.12	2.91	2.61
plane	(002)	(202)	(110)	(402)	(600)	(-312)	(204)

Table 2. *Lattice parameters of terephthalic acid and ammonium terephthalate.*

Material	***Crystal structure***	***Lattice parameters***
Terephthalic acid	Triclinic	a = 6.43 Å, b = 7.39 Å, c = 3.73Å α = 99.37°, β = 91.51°, γ = 83.23°
Ammonium terephthalate	Monoclinic	a = 18.92 Å, b = 3.79 Å, c = 11.48 Å α = γ = 90°, β = 97.44°

3.4. TGA-MS analysis

Thermogravimetric analysis (TGA) of untreated terephthalic acid and terephthalic acid treated by DBD are presented in figure 5. The TGA curves of the two materials (fig. 5a) show that both samples present the same thermal stability, the total loss of the two materials occurs at ~ 325 °C. Moreover, for terephthalic acid, the weight loss occurs in one-step between 250 °C and 325 °C, as shown by the DTG curve (fig. 5b). This weight loss corresponds to the total degradation of the material. In the case of terephthalic acid treated by DBD, the weight loss occurs in two steps. The first one relatively low of 0.9 % is between 125 °C and 165 °C, and the second one, like terephthalic acid pristine, takes place between 250 °C and 325 °C, as seen in figure 5c, which corresponds to the total degradation of the material. To determine the origin of the first mass loss in terephthalic acid treated by DBD, mass spectrometry analysis was carried out during TGA. The analysis reveals that the first weight loss is assigned to the detected masses m/z = 15 and m/z = 16 (fig. 5c), with a threshold temperature T_{th} of 142°C and a maximum degassing temperature T_d at 162°C. This indicates that the first weight loss can be attributed to the degassing of NH and NH_2 amino groups, respectively.

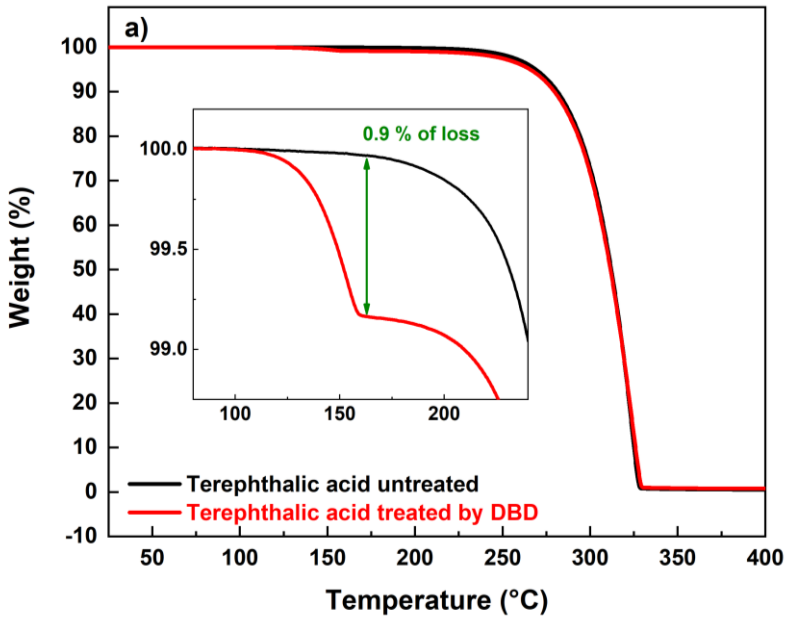

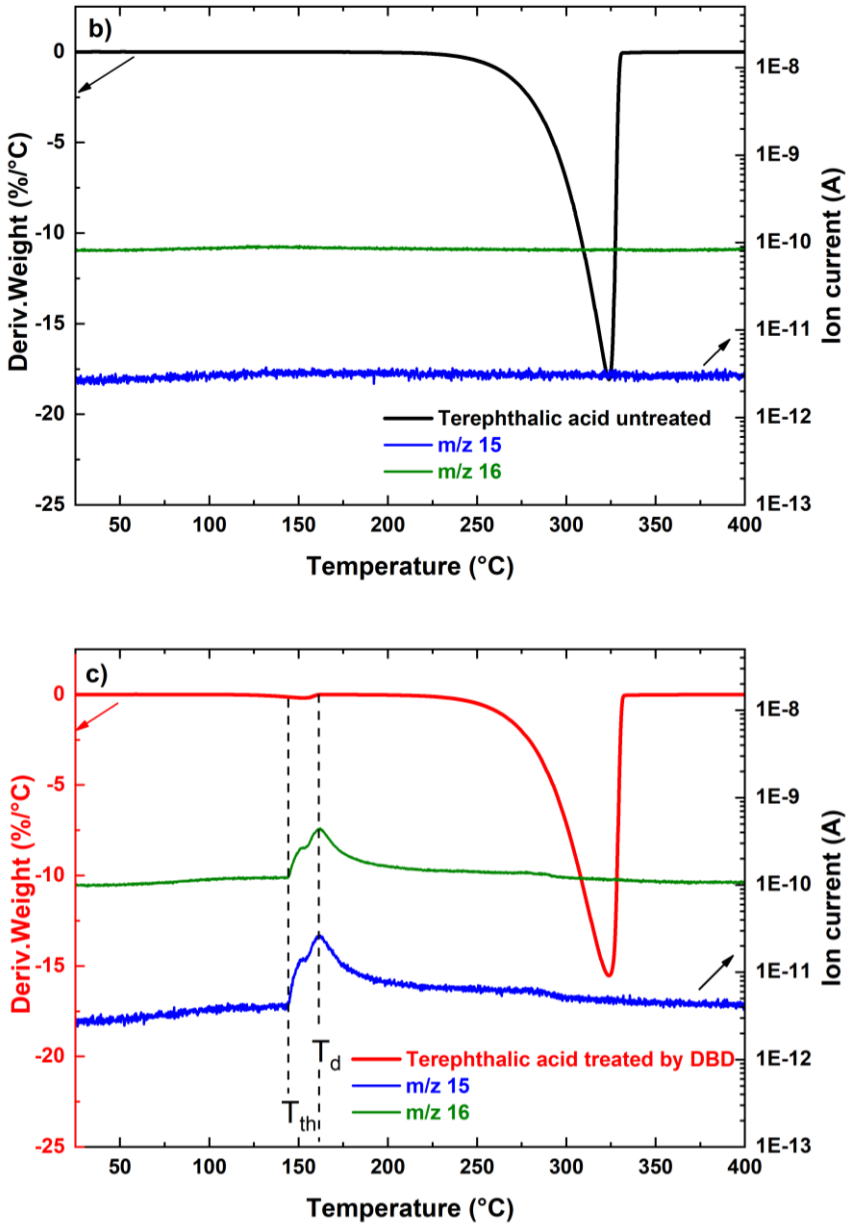

Figure 5: a. *TGA curves of terephthalic acid and terephthalic acid treated by DBD,* ***b.*** *DTG-MS curves of terephthalic acid untreated,* ***c.*** *DTG-MS curves of terephthalic acid treated by DBD.*

3.5. X-Ray photoelectron spectroscopy (XPS)

The XPS survey spectra of both untreated and DBD-processed terephthalic acid are shown in figure 6a. The survey spectra reveal the presence of C and O in the untreated material, and the presence of N in addition to C and O in the terephthalic acid treated by DBD. A variation of atomic percentage (at%) of carbon and oxygen between the two samples was checked. The data

of the individual contributions within the high-resolution spectra are reported in table 3. The global peaks of C_{1s} (fig 6b) and O_{1s} (fig 6c) reveal a clear shift between the untreated and treated material. Moreover, the N_{1s} (fig 6d) peak clearly proves the presence of nitrogen in terephthalic acid treated by DBD, in contrary to terephthalic acid untreated where no nitrogen is detected. The different chemical contributions of each peak were determined in order to understand the origin of the shift observed between the two materials in C_{1s} and O_{1s} peaks. The C_{1s} spectrum of the untreated terephthalic acid (fig 7a) display contributions at 284.8 eV and 289.2 eV, resulting from the C-C (sp^2) and carboxyl C(=O)-O moieties, respectively. In the case of terephthalic acid treated by DBD, a clear change in the chemical structure is shown in the C_{1s} spectrum (fig. 7b). Besides the contributions of C-C and C=(O)-C as for the pristine material, the C_{1s} spectrum of the treated material shows contributions at 285.4 eV, 288.3 eV, corresponding to C-N and C(=O)-N moieties. Moreover, comparison of the two spectra points out a decrease in the C-C and C=O bonds in favour of the C-N and C(=O)-N bonds, respectively, which explains the shift previously mentioned of 0.6 eV toward lower binding energy around 289 eV in the spectrum of terephthalic acid treated by DBD (fig 6b). For O_{1s} spectra (fig 7c, d), both samples reveal two main contributions, arising from the O=C and O-C moieties. Moreover, the O_{1s} spectrum of the organic ligand treated by DBD reveals a third contribution around 531 eV that could be attributed to O=C-N moieties. Therefore, the previous observed shift of 0.5 eV between the two samples (fig. 6c) is related to the presence of a third contribution in the spectrum of terephthalic acid treated by DBD. Regarding N_{1s} spectrum (fig. 7e), it reveals the presence of two structures: the first one, with a contribution at 401.5 eV, corresponds to ammonium salt, whose phase was previously confirmed by XRD, and the second one, with a contribution at 400.1 eV, corresponds to N-C or N-C=O bonds. XPS analysis thus confirms the capability of DBD plasma treatment to graft amino groups on terephthalic acid ligand. All these data suggest that the grafting takes place at the functional carboxyl group (-COOH) of terephthalic acid, by substituting the C–OH bond by C-NH_2 bond, as depicted in

figure 8. The results obtained by XRD, TGA-MS and XPS are coherent with the first result obtained in section 3.1 dealing with current-voltage characteristics. Indeed, the composition of the material has changed throughout the treatment, which had an impact on the plasma characteristics as above mentionned, which we hypothesized that it could be attributed to the change of the secondary electron emission yield. Consequently, the DBD plasma treatment has shown its efficiency to graft amino groups on the organic ligand, which could be useful to synthesize MOFs with amino-based organic ligands.

Table 3. *XPS data of the chemical elements present in the two samples.*

XPS peak bond	Binding energy (eV)	
	Terephthalic acid untreated	**Terephthalic acid treated by DBD**
C_{1s} C-C	**284.8**	**284.6**
C_{1s} C-N	**-**	**285.4**
C_{1s} C(=O)-N	**-**	**288.3**
C_{1s} C(=O)-O	**289.1**	**289.2**
O_{1s} O=C	**531.8**	**532.2**
O_{1s} O-C	**533.2**	**533.6**
O_{1s}	**-**	**531.1**

O=C-N		
N_{1s} **Ammonium salt** **or N-R_3^+**	**-**	**401.5**
N_{1s} **N-C or N-C=O**	**-**	**400.1**

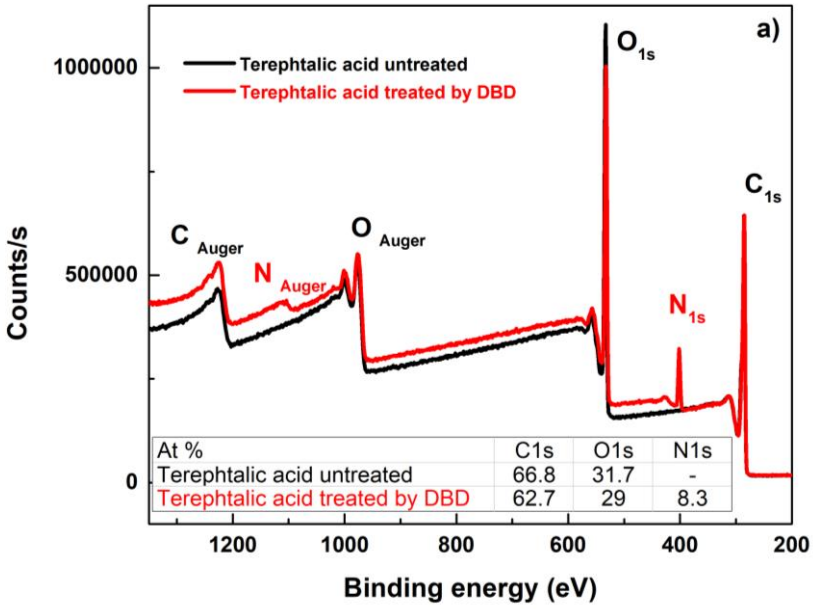

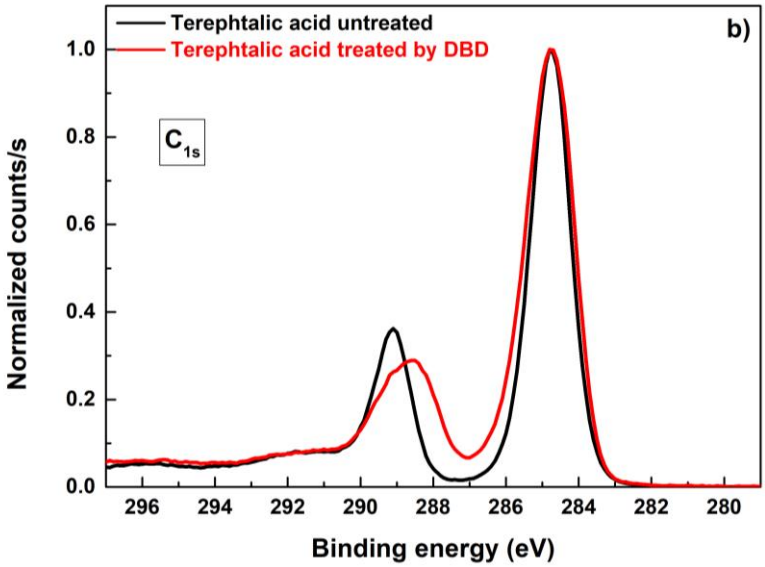

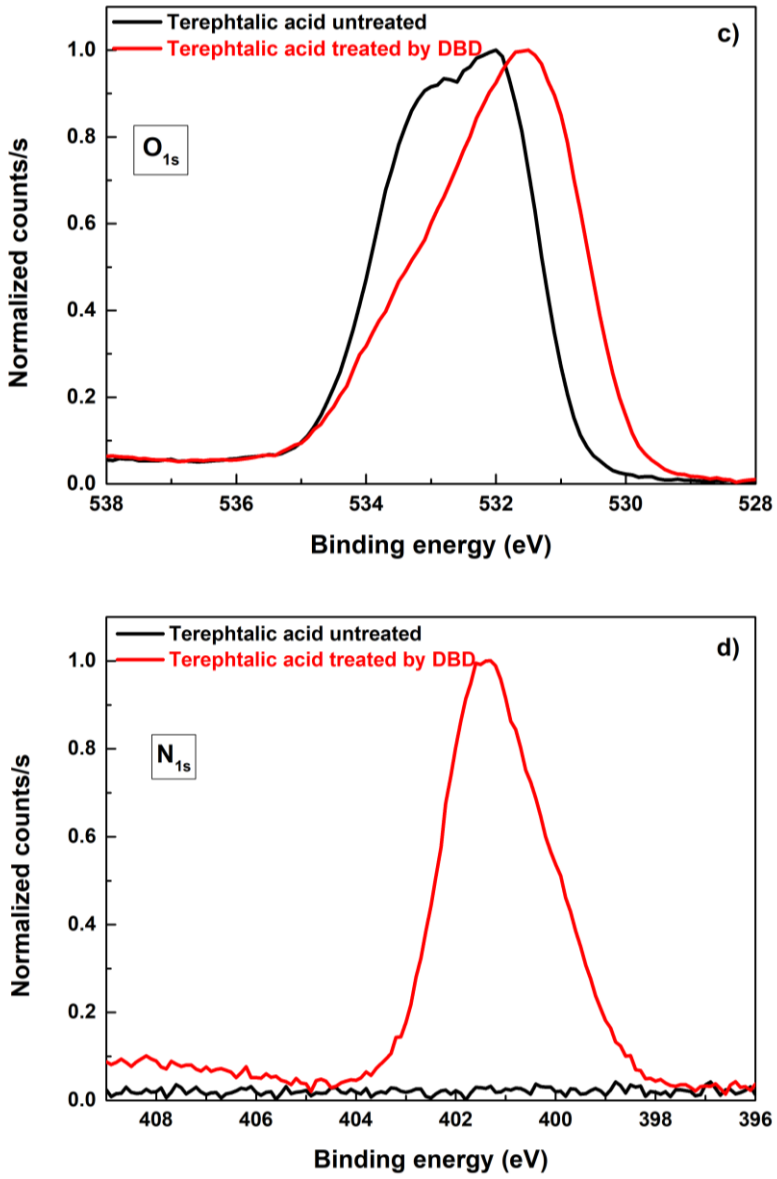

Figure 6: *a. Survey spectra of terephthalic acid untreated and treated by DBD, b. Normalized C_{1s} spectra of terephthalic acid untreated and treated by DBD, c. Normalized O_{1s} spectra of terephthalic acid untreated and treated by DBD, d. Normalized N_{1s} spectra of terephthalic acid untreated and treated by DBD.*

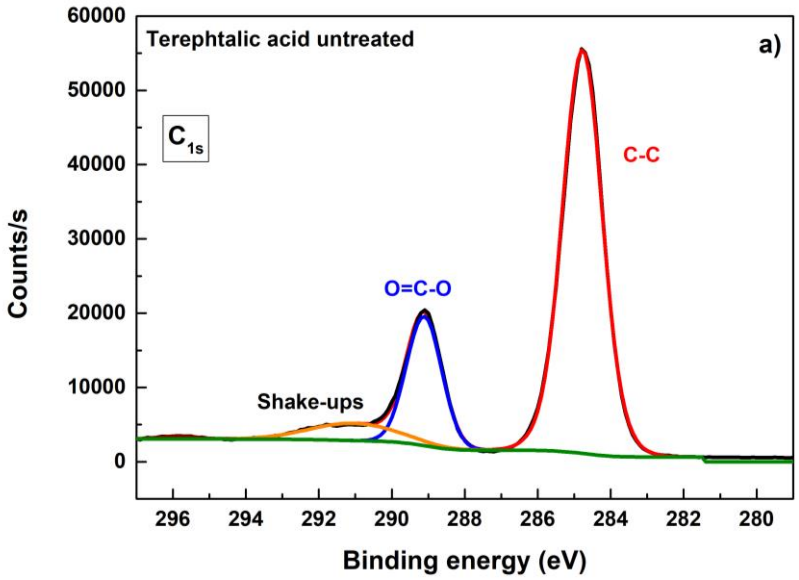
Terephtalic acid untreated
a)
C1s
C-C
O=C-O
Shake-ups
Counts/s
Binding energy (eV)

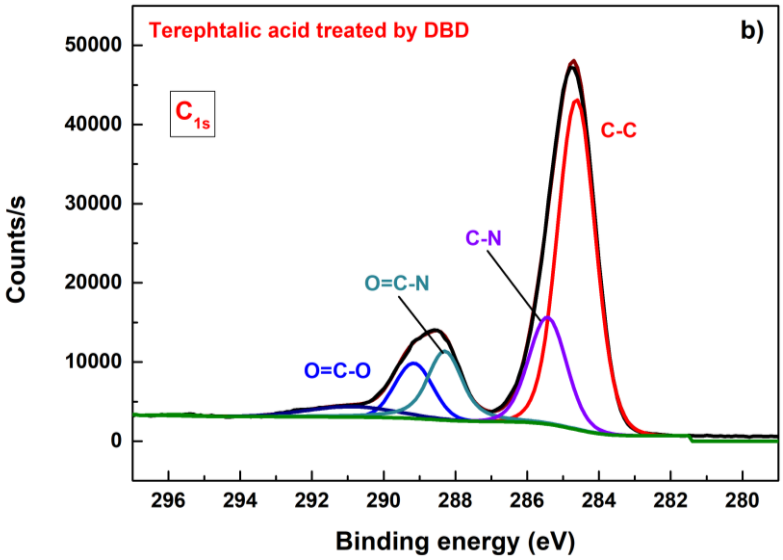
Terephtalic acid treated by DBD
b)
C1s
C-C
C-N
O=C-N
O=C-O
Counts/s
Binding energy (eV)

.

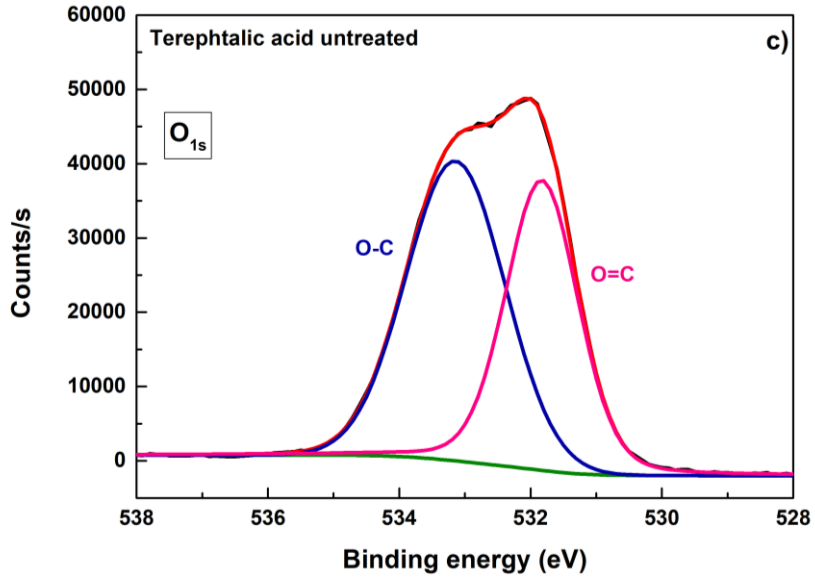
Terephtalic acid untreated
c)
O1s
O-C
O=C
Counts/s
Binding energy (eV)

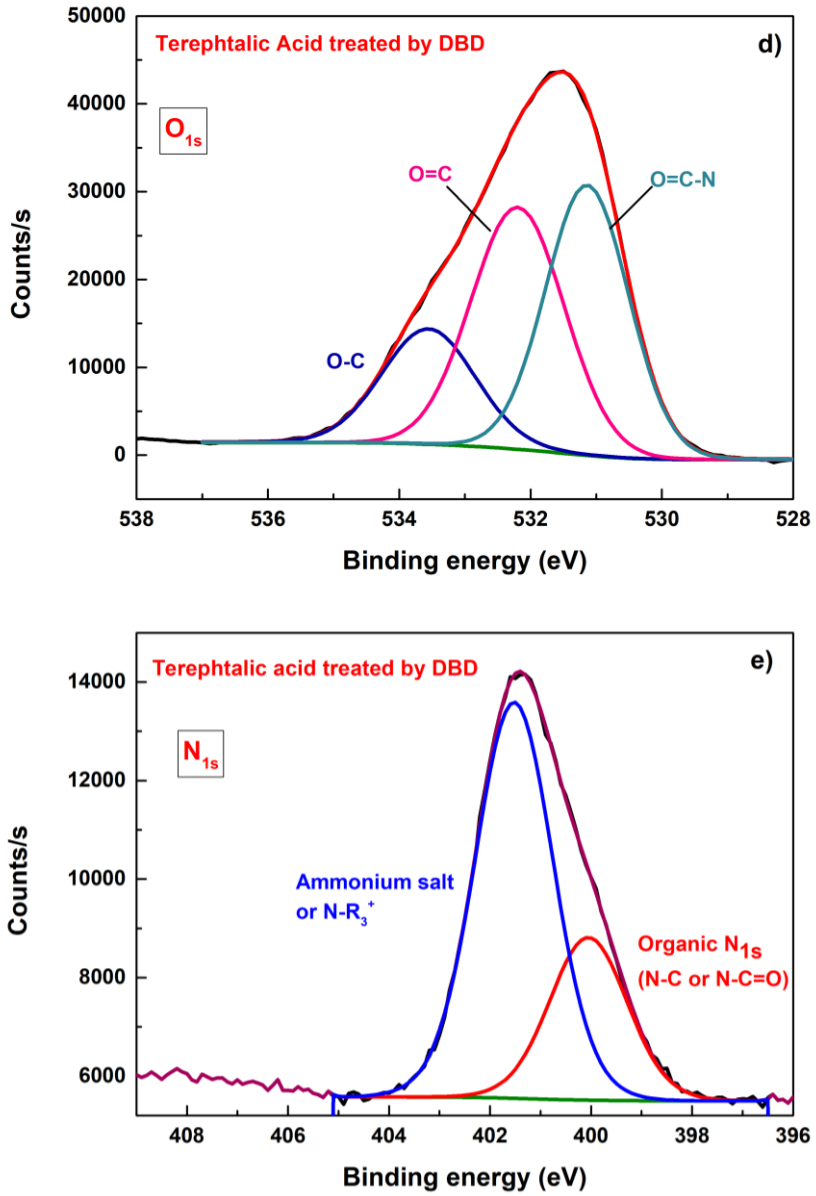

Figure 7: *a. C_{1s} spectrum of terephthalic acid untreated, b. C_{1s} spectrum of terephthalic acid treated by DBD, c. O_{1s} spectrum of terephthalic acid untreated, d. O_{1s} spectrum of terephthalic acid treated by DBD, e. N_{1s} spectrum of terephthalic acid treated by DBD.*

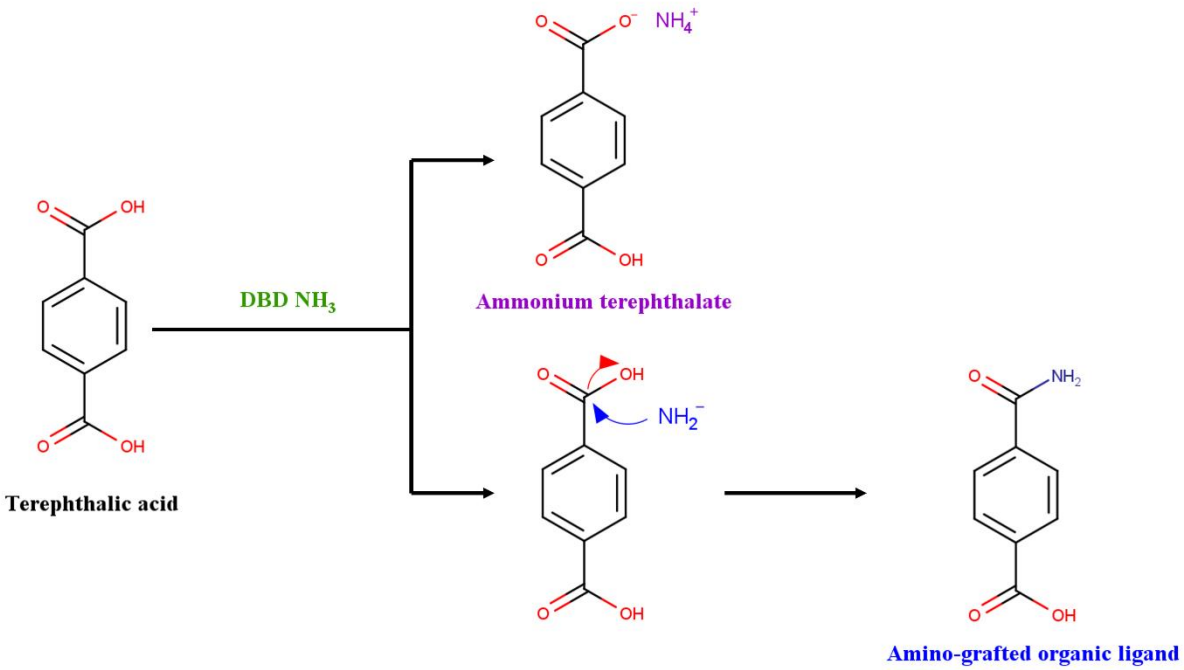

Figure 8. *Preliminary proposed mechanism for the functionalization of terephthalic acid by DBD treatment.*

4. Conclusion

In this work, an amino pre-functionalization study of terephthalic acid ligand by a NH_3 DBD plasma treatment are investigated. The different diagnostic and characterization techniques performed in the present study demonstrate the effectiveness of the DBD plasma treatment to graft amino groups into the organic ligand. The plasma diagnostics reveal the short duration of the DBD discharge, the stability of the plasma treatment over the process time, and the presence of nitrogen-containing radicals in the discharge, especially N_2 and NH. X-Ray diffraction pattern of terephthalic acid treated by DBD reveals the presence of an ammonium hydrogen terephthalate phase together with the phase of untreated terephthalic acid, thus showing that the material undergoes structural modification due to the DBD treatment. TGA-MS curves show that untreated terephthalic acid and terephthalic acid treated by DBD have the same thermal stability (total loss at ~325 °C). DTG measurements show that terephthalic acid treated by DBD exhibits two weight loss steps; the first slight loss of 0.9 % in mass around 125 °C-160 °C is

attributed to the degassing of amino groups (NH, NH_2). The second loss, as for terephthalic acid untreated, occur between 250 °C and 325 °C and is assigned to the total deterioration of the material. XPS analyses show the presence of nitrogen in the material treated by DBD and evidence that the grafting of the amino group occurs at the functional carboxyl group (-COOH) of terephthalic acid by substituting the C–OH bond by C-NH_2 bond. This proves the capacity of the DBD plasma treatment to perform pre-functionalization by grafting amino groups on the organic ligand, which could be useful to synthesize MOFs with amino-based organic ligands.

References

[1] Q. Wang, D. Astruc, State of the Art and Prospects in Metal–Organic Framework (MOF)-Based and MOF-Derived Nanocatalysis, Chem. Rev. 120 (2020) 1438–1511. https://doi.org/10.1021/acs.chemrev.9b00223.

[2] S. Yuan, L. Feng, K. Wang, J. Pang, M. Bosch, C. Lollar, Y. Sun, J. Qin, X. Yang, P. Zhang, Q. Wang, L. Zou, Y. Zhang, L. Zhang, Y. Fang, J. Li, H. Zhou, Stable Metal–Organic Frameworks: Design, Synthesis, and Applications, Adv. Mater. 30 (2018) 1704303. https://doi.org/10.1002/adma.201704303.

[3] M. Li, D. Li, M. O'Keeffe, O.M. Yaghi, Topological Analysis of Metal–Organic Frameworks with Polytopic Linkers and/or Multiple Building Units and the Minimal Transitivity Principle, Chem. Rev. 114 (2014) 1343–1370. https://doi.org/10.1021/cr400392k.

[4] H. Wang, Q.-L. Zhu, R. Zou, Q. Xu, Metal-Organic Frameworks for Energy Applications, Chem. 2 (2017) 52–80. https://doi.org/10.1016/j.chempr.2016.12.002.

[5] M.K. Taylor, T. Runčevski, J. Oktawiec, M.I. Gonzalez, R.L. Siegelman, J.A. Mason, J. Ye, C.M. Brown, J.R. Long, Tuning the Adsorption-Induced Phase Change in the Flexible Metal–Organic Framework Co(bdp), J. Am. Chem. Soc. 138 (2016) 15019–15026. https://doi.org/10.1021/jacs.6b09155.

[6] Y. He, W. Zhou, G. Qian, B. Chen, Methane storage in metal–organic frameworks, Chem. Soc. Rev. 43 (2014) 5657–5678. https://doi.org/10.1039/C4CS00032C.

[7] Q. Qian, P.A. Asinger, M.J. Lee, G. Han, K. Mizrahi Rodriguez, S. Lin, F.M. Benedetti, A.X. Wu, W.S. Chi, Z.P. Smith, MOF-Based Membranes for Gas Separations, Chem. Rev. 120 (2020) 8161–8266. https://doi.org/10.1021/acs.chemrev.0c00119.

[8] H. Noh, Y. Cui, A.W. Peters, D.R. Pahls, M.A. Ortuño, N.A. Vermeulen, C.J. Cramer, L. Gagliardi, J.T. Hupp, O.K. Farha, An Exceptionally Stable Metal–Organic Framework Supported Molybdenum(VI) Oxide Catalyst for Cyclohexene Epoxidation, J. Am. Chem. Soc. 138 (2016) 14720–14726. https://doi.org/10.1021/jacs.6b08898.

[9] Y. Xu, X. Xiao, Z.-M. Ye, S. Zhao, C.-T. He, J.-P. Zhang, Y. Li, X.-M. Chen, A Cage-confinement Pyrolysis Route to Ultrasmall Tungsten Carbide Nanoparticles for Efficient Hydrogen Evolution, Journal of the American Chemical Society. (n.d.) 6. https://doi.org/10.1021/jacs.7b00165.

[10] Y. Zhang, X. Yang, H.-C. Zhou, Synthesis of MOFs for heterogeneous catalysis via linker design, Polyhedron. 154 (2018) 189–201. https://doi.org/10.1016/j.poly.2018.07.021.

[11] C. Gogoi, A. Kumar, M. Sk, S. Biswas, Specific fluorescence sensing of hydrogen sulphide by an azide functionalized Zr(IV) MOF with DUT-52 topology, Microporous and Mesoporous Materials. 311 (2021) 110725. https://doi.org/10.1016/j.micromeso.2020.110725.

[12] S.-N. Zhao, G. Wang, D. Poelman, P. Voort, Luminescent Lanthanide MOFs: A Unique Platform for Chemical Sensing, Materials. 11 (2018) 572. https://doi.org/10.3390/ma11040572.

[13] E.-X. Chen, H. Yang, J. Zhang, Zeolitic Imidazolate Framework as Formaldehyde Gas Sensor, Inorg. Chem. 53 (2014) 5411–5413. https://doi.org/10.1021/ic500474j.

[14] L.R. Mingabudinova, A.S. Zalogina, A.A. Krasilin, M.I. Petrova, P. Trofimov, Y.A. Mezenov, E.V. Ubyivovk, P. Lönnecke, A. Nominé, J. Ghanbaja, T. Belmonte, V.A. Milichko, Laser printing of optically resonant hollow crystalline carbon nanostructures from 1D and 2D metal–organic frameworks, Nanoscale. 11 (2019) 10155–10159. https://doi.org/10.1039/C9NR02167A.

[15] N.L.P. Andrews, J.Z. Fan, R.L. Forward, M.C. Chen, H.-P. Loock, Determination of the thermal, oxidative and photochemical degradation rates of scintillator liquid by fluorescence EEM spectroscopy, Phys. Chem. Chem. Phys. 19 (2017) 73–81. https://doi.org/10.1039/C6CP06015C.

[16] N.K. Kulachenkov, D. Sun, Y.A. Mezenov, A.N. Yankin, S. Rzhevskiy, V. Dyachuk, A. Nominé, G. Medjahdi, E.A. Pidko, V.A. Milichko, Photochromic Free MOF-Based Near-Infrared Optical Switch, Angew. Chem. Int. Ed. 59 (2020) 15522–15526. https://doi.org/10.1002/anie.202004293.

[17] Z. Wang, J. Hu, L. Han, Z. Wang, H. Wang, Q. Zhao, J. Liu, F. Pan, A MOF-based single-ion Zn2+ solid electrolyte leading to dendrite-free rechargeable Zn batteries, Nano Energy. 56 (2019) 92–99.

https://doi.org/10.1016/j.nanoen.2018.11.038.

[18] X. Hu, Z. Zhu, F. Cheng, Z. Tao, J. Chen, Micro-nano structured Ni-MOFs as high-performance cathode catalyst for rechargeable Li–O $_2$ batteries, Nanoscale. 7 (2015) 11833–11840.
https://doi.org/10.1039/C5NR02487K.

[19] G. de Combarieu, M. Morcrette, F. Millange, N. Guillou, J. Cabana, C.P. Grey, I. Margiolaki, G. Férey, J.-M. Tarascon, Influence of the Benzoquinone Sorption on the Structure and Electrochemical Performance of the MIL-53(Fe) Hybrid Porous Material in a Lithium-Ion Battery, Chem. Mater. 21 (2009) 1602–1611.
https://doi.org/10.1021/cm8032324.

[20] J. Ren, N.M. Musyoka, H.W. Langmi, B.C. North, M. Mathe, X. Kang, S. Liao, Hydrogen storage in Zr-fumarate MOF, International Journal of Hydrogen Energy. 40 (2015) 10542–10546.
https://doi.org/10.1016/j.ijhydene.2015.06.109.

[21] F. Ragon, B. Campo, Q. Yang, C. Martineau, A.D. Wiersum, A. Lago, V. Guillerm, C. Hemsley, J.F. Eubank, M. Vishnuvarthan, F. Taulelle, P. Horcajada, A. Vimont, P.L. Llewellyn, M. Daturi, S. Devautour-Vinot, G. Maurin, C. Serre, T. Devic, G. Clet, Acid-functionalized UiO-66(Zr) MOFs and their evolution after intra-framework cross-linking: structural features and sorption properties, J. Mater. Chem. A. 3 (2015) 3294–3309. https://doi.org/10.1039/C4TA03992K.

[22] R. Rani, A. Deep, B. Mizaikoff, S. Singh, Enhanced hydrothermal stability of Cu MOF by post synthetic modification with amino acids, Vacuum. 164 (2019) 449–457. https://doi.org/10.1016/j.vacuum.2019.01.011.

[23] M. Eddaoudi, J. Kim, N. Rosi, D. Vodak, J. Wachter, M. O'Keeffe, O.M. Yaghi, Systematic Design of Pore Size and Functionality in Isoreticular MOFs and Their Application in Methane Storage, Science. 295 (2002) 469–472.
https://doi.org/10.1126/science.1067208.

[24] T. Devic, P. Horcajada, C. Serre, F. Salles, G. Maurin, B. Moulin, D. Heurtaux, G. Clet, A. Vimont, J.-M. Grenèche, B.L. Ouay, F. Moreau, E. Magnier, Y. Filinchuk, J. Marrot, J.-C. Lavalley, M. Daturi, G. Férey, Functionalization in Flexible Porous Solids: Effects on the Pore Opening and the Host−Guest Interactions, J. Am. Chem. Soc. 132 (2010) 1127–1136. https://doi.org/10.1021/ja9092715.

[25] B.F. Hoskins, R. Robson, Design and Construction of a New Class of Scaffolding-like Materials Comprising Infinite Polymeric Frameworks of 3D-Linked Molecular Rods. A Reappraisal of the $Zn(CN)_2$ and $Cd(CN)_2$ Structures and the Synthesis and Structure of the Diamond-Related Frameworks $[N(CH_3)_4][Cu^{I}Zn^{II}(CN)_4]$ and CU^{I}[4,4"4",4"'-tetracyanotetraphenylmethane] $BF_4.xC_6H_5NO_2$,''. J. Am. Chem. Soc. 112 (1990) 1546–1554. https://doi.org/10.1021/ja00160a038.

[26] Z. Wang, S.M. Cohen, Postsynthetic Covalent Modification of a Neutral Metal−Organic Framework, J. Am. Chem. Soc. 129 (2007) 12368–12369. https://doi.org/10.1021/ja074366o.

[27] M. Kandiah, S. Usseglio, S. Svelle, U. Olsbye, K.P. Lillerud, M. Tilset, Post-synthetic modification of the metal–organic framework compound UiO-66, J. Mater. Chem. 20 (2010) 9848. https://doi.org/10.1039/c0jm02416c.

[28] S. Chen, Z. Song, J. Lyu, Y. Guo, B.E.G. Lucier, W. Luo, M.S. Workentin, X. Sun, Y. Huang, Anhydride Post-Synthetic Modification in a Hierarchical Metal–Organic Framework, J. Am. Chem. Soc. 142 (2020) 4419–4428. https://doi.org/10.1021/jacs.9b13414.

[29] W. Dong, L. Yang, Y. Huang, Glycine post-synthetic modification of MIL-53(Fe) metal–organic framework with enhanced and stable peroxidase-like activity for sensitive glucose biosensing, Talanta. 167 (2017) 359–366. https://doi.org/10.1016/j.talanta.2017.02.039.

[30] C.-D. Wu, A. Hu, L. Zhang, W. Lin, A Homochiral Porous Metal−Organic Framework for Highly Enantioselective Heterogeneous Asymmetric Catalysis, J. Am. Chem. Soc. 127 (2005) 8940–8941. https://doi.org/10.1021/ja052431t.

[31] G. Li, H. Kobayashi, J.M. Taylor, R. Ikeda, Y. Kubota, K. Kato, M. Takata, T. Yamamoto, S. Toh, S. Matsumura, H. Kitagawa, Hydrogen storage in Pd nanocrystals covered with a metal–organic framework, Nature Mater. 13 (2014) 802–806. https://doi.org/10.1038/nmat4030.

[32] Q. Yang, A.D. Wiersum, P.L. Llewellyn, V. Guillerm, C. Serre, G. Maurin, Functionalizing porous zirconium terephthalate UiO-66(Zr) for natural gas upgrading: a computational exploration, Chem. Commun. 47 (2011) 9603. https://doi.org/10.1039/c1cc13543k.

[33] S. Couck, J.F.M. Denayer, G.V. Baron, T. Rémy, J. Gascon, F. Kapteijn, An Amine-Functionalized MIL-53 Metal−Organic Framework with Large Separation Power for CO_2 and CH_4, J. Am. Chem. Soc. 131 (2009) 6326–6327. https://doi.org/10.1021/ja900555r.

[34] L. Wu, M. Xue, S.-L. Qiu, G. Chaplais, A. Simon-Masseron, J. Patarin, Amino-modified MIL-68(In) with enhanced hydrogen and carbon dioxide sorption enthalpy, Microporous and Mesoporous Materials. 157 (2012) 75–81. https://doi.org/10.1016/j.micromeso.2011.12.034.

[35] Z.H. Rada, H.R. Abid, J. Shang, Y. He, P. Webley, S. Liu, H. Sun, S. Wang, Effects of amino functionality on uptake of CO2, CH4 and selectivity of CO2/CH4 on titanium based MOFs, Fuel. 160 (2015) 318–327. https://doi.org/10.1016/j.fuel.2015.07.088.

[36] O. Hübner, A. Glöss, M. Fichtner, W. Klopper, On the Interaction of Dihydrogen with Aromatic Systems, J. Phys. Chem. A. 108 (2004) 3019–3023. https://doi.org/10.1021/jp031102p.

[37] B. Liu, M. Jiang, D. Zhu, J. Zhang, G. Wei, Metal-organic frameworks functionalized with nucleic acids and amino acids for structure- and function-specific applications: A tutorial review, Chemical Engineering Journal. 428 (2022) 131118. https://doi.org/10.1016/j.cej.2021.131118.

[38] W.-H. Chen, X. Yu, A. Cecconello, Y.S. Sohn, R. Nechushtai, I. Willner, Stimuli-responsive nucleic acid-functionalized metal–organic framework nanoparticles using pH- and metal-ion-dependent DNAzymes as locks, Chem. Sci. 8 (2017) 5769–5780. https://doi.org/10.1039/C7SC01765K.

[39] J.S. Kahn, L. Freage, N. Enkin, M.A.A. Garcia, I. Willner, Stimuli-Responsive DNA-Functionalized Metal-Organic Frameworks (MOFs), Adv. Mater. 29 (2017) 1602782. https://doi.org/10.1002/adma.201602782.

[40] S. Lin, N. Gan, Y. Cao, Y. Chen, Q. Jiang, Selective dispersive solid phase extraction-chromatography tandem mass spectrometry based on aptamer-functionalized UiO-66-NH2 for determination of polychlorinated biphenyls, Journal of Chromatography A. 1446 (2016) 34–40. https://doi.org/10.1016/j.chroma.2016.04.016.

[41] R. Newar, N. Akhtar, N. Antil, A. Kumar, S. Shukla, W. Begum, K. Manna, Amino Acid-Functionalized Metal-Organic Frameworks for Asymmetric Base–Metal Catalysis, Angew. Chem. Int. Ed. 60 (2021) 10964–10970. https://doi.org/10.1002/anie.202100643.

[42] J. Canivet, S. Aguado, G. Bergeret, D. Farrusseng, Amino acid functionalized metal–organic frameworks by a soft coupling–deprotection sequence, Chem. Commun. 47 (2011) 11650.
https://doi.org/10.1039/c1cc15541e.

[43] L. Lili, Z. Xin, R. Shumin, Y. Ying, D. Xiaoping, G. Jinsen, X. Chunming, H. Jing, Catalysis by metal–organic frameworks: proline and gold functionalized MOFs for the aldol and three-component coupling reactions, RSC Adv. 4 (2014) 13093–13107. https://doi.org/10.1039/C4RA01269K.

[44] M.M. Pires, D.E. Przybyla, J. Chmielewski, A Metal-Collagen Peptide Framework for Three-Dimensional Cell Culture, Angew. Chem. Int. Ed. 48 (2009) 7813–7817. https://doi.org/10.1002/anie.200902375.

[45] N.K. Maddigan, A. Tarzia, D.M. Huang, C.J. Sumby, S.G. Bell, P. Falcaro, C. J. Doonan, Protein surface functionalisation as a general strategy for facilitating biomimetic mineralisation of zif-8, Chem. Sci. 9 (2018) 4217–4223.
https://doi.org/10.1039/C8SC00825F.

[46] M. Can, S. Demirci, A.K. Sunol, N. Sahiner, An amino acid, l-Glutamic acid-based metal-organic frameworks and their antibacterial, blood compatibility, biocompatibility, and sensor properties, Microporous and Mesoporous Materials. 309 (2020) 110533. https://doi.org/10.1016/j.micromeso.2020.110533.

[47] R. Laurano, M. Boffito, A. Torchio, C. Cassino, V. Chiono, G. Ciardelli, Plasma Treatment of Polymer Powder as an Effective Tool to Functionalize Polymers: Case Study Application on an Amphiphilic Polyurethane, Polymers. 11 (2019) 2109. https://doi.org/10.3390/polym11122109.

[48] M. Shahpanah, S. Mehrabian, M. Abbasi-Firouzjah, B. Shokri, Improving the oxygen barrier properties of PET polymer by radio frequency plasma-polymerized SiOxNy thin film, Surface and Coatings Technology. 358 (2019) 91–97.
https://doi.org/10.1016/j.surfcoat.2018.11.023.

[49] K.G. Kostov, Y.A.A. Hamia, R.P. Mota, A.L.R. dos Santos, P.A.P. Nascente, Treatment of polycarbonate by dielectric barrier discharge (DBD) at atmospheric pressure, J. Phys.: Conf. Ser. 511 (2014) 012075.
https://doi.org/10.1088/1742-6596/511/1/012075.

[50] F. Sohbatzadeh, M. Farhadi, E. Shakerinasab, A new DBD apparatus for super-hydrophobic coating deposition on cotton fabric, Surface and Coatings Technology. 374 (2019) 944–956.

https://doi.org/10.1016/j.surfcoat.2019.06.086.

[51] J. Yang, Y. Pu, D. Miao, X. Ning, Fabrication of Durably Superhydrophobic Cotton Fabrics by Atmospheric Pressure Plasma Treatment with a Siloxane Precursor, Polymers. 10 (2018) 460.
https://doi.org/10.3390/polym10040460.

[52] I. Belhaj Khalifa, N. Ladhari, Hydrophobic behavior of cotton fabric activated with air atmospheric-pressure plasma, The Journal of The Textile Institute. 111 (2020) 1191–1197. https://doi.org/10.1080/00405000.2019.1688907.

[53] G. Avramidis, E. Hauswald, A. Lyapin, H. Militz, W. Viöl, A. Wolkenhauer, Plasma treatment of wood and wood-based materials to generate hydrophilic or hydrophobic surface characteristics, Wood Material Science & Engineering. 4 (2009) 52–60. https://doi.org/10.1080/17480270903281642.

[54] L. Xie, Z. Tang, L. Jiang, V. Breedveld, D.W. Hess, Creation of superhydrophobic wood surfaces by plasma etching and thin-film deposition, Surface and Coatings Technology. 281 (2015) 125–132.
https://doi.org/10.1016/j.surfcoat.2015.09.052.

[55] J. Profili, O. Levasseur, A. Koronai, L. Stafford, N. Gherardi, Deposition of nanocomposite coatings on wood using cold discharges at atmospheric pressure, Surface and Coatings Technology. 309 (2017) 729–737.
https://doi.org/10.1016/j.surfcoat.2016.10.095.

[56] R. Múgica-Vidal, F. Alba-Elías, E. Sainz-García, M. Pantoja-Ruiz, Atmospheric pressure air plasma treatment of glass substrates for improved silver/glass adhesion in solar mirrors, Solar Energy Materials and Solar Cells. 169 (2017) 287–296. https://doi.org/10.1016/j.solmat.2017.05.034.

[57] M. Gao, Y. Wang, Y. Zhang, Y. Li, Y. Tang, Y. Huang, Deposition of thin films on glass fiber fabrics by atmospheric pressure plasma jet, Surface and Coatings Technology. 404 (2020) 126498.
https://doi.org/10.1016/j.surfcoat.2020.126498.

[58] B. Garrido, I.G. Cano, S. Dosta, Adhesion improvement and in vitro characterisation of 45S5 bioactive glass coatings obtained by atmospheric plasma spraying, Surface and Coatings Technology. 405 (2021) 126560.
https://doi.org/10.1016/j.surfcoat.2020.126560.

[59] B. Brzhozovskii, M. Brovkova, I. Gots, H. Zinina, V. Martynov, Study of the low-temperature plasma treatment effect on the structure, physical and chemical surface

characteristics of 40X13 steel, Heliyon. 5 (2019) e02388. https://doi.org/10.1016/j.heliyon.2019.e02388.

[60] M.C. Kim, S.H. Yang, J.-H. Boo, J.G. Han, Surface treatment of metals using an atmospheric pressure plasma jet and their surface characteristics, Surface and Coatings Technology. 174–175 (2003) 839–844. https://doi.org/10.1016/S0257-8972(03)00560-7.

[61] J. Martin, P. Haraux, V. Ntomprougkidis, S. Migot, S. Bruyère, G. Henrion, Characterization of metal oxide micro/nanoparticles elaborated by plasma electrolytic oxidation of aluminium and zirconium alloys, Surface and Coatings Technology. 397 (2020) 125987. https://doi.org/10.1016/j.surfcoat.2020.125987.

[62] A. Malesevic, R. Vitchev, K. Schouteden, A. Volodin, L. Zhang, G.V. Tendeloo, A. Vanhulsel, C.V. Haesendonck, Synthesis of few-layer graphene via microwave plasma-enhanced chemical vapour deposition, Nanotechnology. 19 (2008) 305604. https://doi.org/10.1088/0957-4484/19/30/305604.

[63] P. Brault, A. Caillard, S. Baranton, M. Mougenot, S. Cuynet, C. Coutanceau, One-step Synthesis and Chemical Characterization of Pt-C Nanowire Composites by Plasma Sputtering, ChemSusChem. 6 (2013) 1168–1171. https://doi.org/10.1002/cssc.201300236.

[64] H.-S. Tsai, C.-C. Lai, H. Medina, S.-M. Lin, Y.-C. Shih, Y.-Z. Chen, J.-H. Liang, Y.-L. Chueh, Scalable graphene synthesised by plasma-assisted selective reaction on silicon carbide for device applications, Nanoscale. 6 (2014) 13861–13869. https://doi.org/10.1039/C4NR04486J.

[65] T. Abuzairi, M. Nagatsu, N.R. Poespawati, R.W. Purnamaningsih, M. Okada, Y. Mochizuki, Atmospheric pressure plasma functionalization of carbon nanotube dot-array with two-stage plasma treatments for the development of bio-chip sensors, in: 2015 International Conference on Quality in Research (QiR), IEEE, Lombok, Indonesia, 2015: pp. 16–18. https://doi.org/10.1109/QiR.2015.7374885.

[66] S. Samukawa, M. Hori, S. Rauf, K. Tachibana, P. Bruggeman, G. Kroesen, J.C. Whitehead, A.B. Murphy, A.F. Gutsol, S. Starikovskaia, U. Kortshagen, J.-P. Boeuf, T.J. Sommerer, M.J. Kushner, U. Czarnetzki, N. Mason, The 2012 Plasma Roadmap, J. Phys. D: Appl. Phys. 45 (2012) 253001. https://doi.org/10.1088/0022-3727/45/25/253001.

[67] Anders, A. Cathodic arcs: from fractal spots to energetic condensation. Springer, New York 50 (2009).

[68] N. Bundaleska, A. Dias, N. Bundaleski, E. Felizardo, J. Henriques, D. Tsyganov, M. Abrashev, E. Valcheva, J. Kissovski, A.M. Ferraria, A.M.B. do Rego, A. Almeida, J. Zavašnik, U. Cvelbar, O.M.N.D. Teodoro, Th. Strunskus, E. Tatarova, Prospects for microwave plasma synthesized N-graphene in secondary electron emission mitigation applications, Sci Rep. 10 (2020) 13013. https://doi.org/10.1038/s41598-020-69844-9.

[69] R.W.B. Pearse and A.G. Gaydon, The Identification of Molecular Spectra, Chapman and Hall LTD, London, Chapter V 332 (1965).

[70] J.K.G. Watson, W.A. Majewski, J.H. Glownia, Assignment of the Schuster band of ammonia, Journal of Molecular Spectroscopy. 115 (1986) 82–87. https://doi.org/10.1016/0022-2852(86)90277-8.

[71] Y. Yi, R. Zhang, L. Wang, J. Yan, J. Zhang, H. Guo, Plasma-Triggered CH_4 /NH_3 Coupling Reaction for Direct Synthesis of Liquid Nitrogen-Containing Organic Chemicals, ACS Omega. 2 (2017) 9199–9210. https://doi.org/10.1021/acsomega.7b01060.

[72] R.E. Cobbledick, R.W.H. Small, The crystal structure of ammonium hydrogen terephthalate, Acta Crystallogr B Struct Crystallogr Cryst Chem. 28 (1972) 2924–2928. https://doi.org/10.1107/S056774087200723X.